scientific reports

Check for updates

OPEN

# Performance of machine learning algorithms in spectroscopic ellipsometry data analysis of $ZnTiO_3$ nanocomposite

Ali Barkhordari[1]✉, Hamid Reza Mashayekhi[1], Pari Amiri[2,3], Süleyman Özçelik[5,6], Ferhat Hanife[5,6] & Yashar Azizian-Kalandaragh[4,5,6]

**In this research, the optical properties of the PVP: $ZnTiO_3$ nanocomposite are studied using the spectroscopic ellipsometry technique. The preparation procedure of the $ZnTiO_3$ nanocomposite is explained in detail. The absorbance/transmittance, surface morphology, structural information, chemical identification, and surface topography of the $ZnTiO_3$ nanocomposite is studied using UV–Vis spectroscopy, field-emission scanning electron microscopy, Raman spectroscopy, Fourier transform infra-red, and atomic force microscopy, respectively. The ellipsometry method is used to obtain the spectra of the real and imaginary parts of the dielectric function and refractive index in the photon energy range of 0.59–4.59 eV. Moreover, using two machine learning algorithms, namely artificial neural network and support vector regression methods, the ellipsometric parameters ψ and Δ are analyzed and compared with non-linear regression. The error and accuracy of each three methods, as well as the time required for their execution, are calculated to compare their suitability in the ellipsometric data analysis. Also, the absorption coefficient was used to determine the band gap energy of the $ZnTiO_3$ nanocomposite, which is found to be 3.83 eV. The second-energy derivative of the dielectric function is utilized to identify six critical point energies of the prepared sample. Finally, the spectral-dependent optical loss function and optical conductivity of the $ZnTiO_3$ nanocomposite are investigated.**

Recently, metal oxides have been extensively utilized as semiconductor materials in various fields such as non-linear optics, optoelectronics[1], electronics, power storage devices[2], catalysts[3], etc. So far, the photocatalytic response of some of the metal oxide materials including $SnO_2$, $TiO_2$, and ZnO has been studied and it has been found that most of them are only active in the UV range because of their wide band gap[4–6]. Moreover, several perovskite compounds including $BaTiO_3$, $CaTiO_3$, $SrTiO_3$, and $ZnTiO_3$ have been applied in sensors, memory instruments, and as catalyst electrodes in fuel cells, owing to their ferroelectric and piezoelectric features. Because these compounds are non-toxic and chemically stable materials that reveal a good photo reactivity in the visible region, they can be appropriate alternatives for $TiO_2$[7,8].

$ZnTiO_3$ is a composite of ZnO and $TiO_2$ substances, both of which are wideband semiconductors with unique features and many applications[9–11]. ZnO has multiple advantages that have been extensively discussed in the literature, including special qualities and numerous applications in transparent electronics, spin electronics, ultraviolet (UV) light emitters, chemical sensors, and piezoelectric instruments[12–15]. Compared to other materials frequently employed as semiconductors for blue-green light-emitting devices, such as ZnSe (22 meV) and GaN (25 meV), ZnO has an impressive exciton binding energy (60 meV)[16]. On the other hand, $TiO_2$ is a semiconductor that is non-toxic, stable in aqueous solutions, and reasonably priced. The significant photocatalytic feature of the $TiO_2$ substance originates from the wide band gap and long lifetime of photogenerated electron–hole pairs[17]. However, $TiO_2$ does not use as much of the solar spectrum as other photocatalytic materials, and it also exhibits

[1]Faculty of Physics, Shahid Bahonar University of Kerman, Kerman, Iran. [2]Department of Engineering Sciences, University of Mohaghegh Ardabili, Namin, Iran. [3]Department of Engineering Sciences, Faculty of Advanced Technologies, Sabalan University of Advanced Technologies (SUAT), Namin, Iran. [4]Department of Physics, University of Mohaghegh Ardabili, P.O. Box 179, Ardabil, Iran. [5]Department of Photonics, Faculty of Applied Sciences, Gazi University, 06500 Ankara, Turkey. [6]Photonics Application and Research Center, Gazi University, 06500 Ankara, Turkey. ✉email: alibarkhordari20@yahoo.com

a relatively high rate of electron–hole recombination. These problems can be resolved and the activity of $TiO_2$ photocatalysts improved by ZnO doping[18].

Therefore, despite some disadvantages associated with the ZnO and $TiO_2$ materials separately, these issues can be addressed through their combination, known as $ZnTiO_3$. It belongs to the hybrid ZnO-$TiO_2$ system, improving the optical efficiency of $TiO_2$ substance by reducing the charge recombination, altering the energy band gap, and therefore shifting the optical response from UV to visible regions[19,20]. Nonlinear optical and luminous materials[21], Catalysts[22], microwave dielectrics[23], nanofibers[24], phosphors[25], gas sensors[26], white pigments[27], and antibacterial stone coatings[28] are just a few of the numerous uses for $ZnTiO_3$. There are different methods to produce the $ZnTiO_3$-based substances in the form of fibers, mesoporous materials, ceramics, films, and powders such as solid-state reaction[29], chemical bath deposition[30], molten-salt technique[27], radio-frequency sputtering[21], sol–gel procedure[23], and evaporation-induced self-assembly technique[31].

As well known, polymer molecules are long chemical chains. Thin films produced through polymer synthesis have attracted attention due to their numerous advantages, such as high stability, affordability, easy processing, and extensibility[32]. Because of these benefits, polymers are gaining popularity in the electronic and optoelectronic industries[33]. Nevertheless, the utilization of polymers may result in a decrease in electrical conductivity. Doping these polymers with metal/metal oxide nanostructures increases their electrical conductivity. Polyvinylpyrrolidone (PVP) is a non-toxic and non-ionic macropolymer widely used in the synthesis of nanocomposites[34]. Depending on the synthesis procedures and particular material systems, PVP can be used as a growth modifier, surface stabilizer, declining agent, and nanostructure dispersion. Also, it has an appropriate electronic conductivity compared to other polymers[35].

It should be mentioned that the main parameters in the optical characterization of substances are refractive index, extinction coefficient, dielectric functions, band gap energy, and absorption coefficient, known as optical functions. The optical functions measurement is very important due to not only their importance in investigating macroscopic and microscopic materials' characteristics but also in designing and producing optical devices. One of the widely used optical techniques to measure the substances' optical functions is ellipsometry. Ellipsometry, as a non-destructive method, preserves the specimen, but accurately reproducing specimen various materials' optical coefficients is difficult in reality. Mathematically, the determination of optical functions is an inverse problem and there is no possibility for analytical solutions to the inverse ellipsometric problems in general, especially in the problems related to the samples with more than one film on a substrate. So, commonly the regression data fitting methods are utilized to get values of optical parameters that most correspond to the observed data. It is evident that these methods are based on trial and error and without a good initial estimate, achieving convergence in the fitting process is not feasible. Therefore, the intervention of an expert is required to provide an appropriate initial guess. On the other hand, sometimes it is necessary to combine multiple models for an accurate description of a sample, in which the appropriate initial estimate becomes more challenging due to the increased number of correlated fitting parameters. To overcome these problems, using new methods that there is no require for expert intervention is essential. One of the newest applicable methods is Machine Learning (ML).

ML, as a branch of artificial intelligence, was introduced by A. Samuel in 1959[36]. It enables computers to automatically process and classify existing datasets, and data analysis without the need for programming, solely based on certain algorithms. Based on the available information, the machine utilizes a specific algorithm for mathematical modeling of the given complex problem to analyze data. Artificial Neural Network (ANN), as one of the ML algorithms, processes information like the way a human brain processes. ANN includes a large number of neurons that are linked to each other, known as nodes, in various processing units similar to the brain neurons. The ANN layers are known as input, output, and hidden layers. After initial information about the considered topic to study is received in the input layer, analyzing and processing of data is done in one or more hidden layers, and then the results as ANN response are transferred to the output layer. One of the primary attributes of an ANN is its ability to extract significant information from intricate data sets that may contain noise and the ANN algorithm yields output promptly after being trained once in advance. ANN can be applied for both classification and regression purposes and has great applications in economics, forensics, pattern detection, etc. One of the other applicable ML algorithms is the Support Vector Regression (SVR) algorithm. The SVR, which was proposed by Vapnik et al.[37], is a supervised machine-learning technique that is commonly employed for classification and regression tasks. The desirable purpose of the SVR is to construct an optimal decision boundary, referred to as a hyperplane, that in a high dimensional space separates data into various categories. In the SVR, the choice of support vectors as extreme vector points helps to form a convenient hyperplane. The distance between the hyperplane and each class's nearest data points, known as the margin, is maximized and at the same time, the classification errors are minimized. Thereby the accurate classification of data points into their befitting categories gets easier. The SVR algorithm is widely utilized in various domains such as face recognition, text categorization, image classification, self-driving cars, chatbots, etc.

Based on our knowledge and investigations, there is no spectroscopic ellipsometry data of the $ZnTiO_3$ nanocomposite. In this work, the nanostructure and nanocomposite of $ZnTiO_3$ are initially prepared. UV–Vis spectroscopy, field emission scanning electron microscopy (FESEM), Raman spectroscopy, Attenuated Total Reflectance (ATR), Fourier-transform infrared spectroscopy (FTIR), and atomic force microscopy (AFM) are employed to study the absorbance/transmittance, the surface morphology, structural information, chemical identification, and surface topography of the $ZnTiO_3$ nanocomposite, respectively. Next, the optical constants of the $ZnTiO_3$ nanocomposite are determined by the spectroscopic ellipsometry measurement in the photon energy range of 0.59–4.59 eV. To investigate and prove the efficiency of the ML approach for analyzing the ellipsometry parameters ($\psi$ and $\Delta$), the ANN and SVR algorithms are used in the photon energy range of 0.59–4.59 eV. Furthermore, the accuracy and time-needing of the ML methods are calculated to evaluate them and to compare the two methods' efficiency with each other as well as with the non-linear (NL) fitting method. Then, the spectral-dependent optical constants of the $ZnTiO_3$ nanocomposite are calculated by the ellipsometry measurement data.

The energies of the band gap and inter-band transition of the sample are also determined. Eventually, the optical loss function and optical conductivity of the $ZnTiO_3$ nanocomposite will be plotted and discussed.

## Experimental details

### Synthesis of $ZnTiO_3$ nanostructures and preparation of its composite

The precursors of $TiCl_4$ (≥ 99%) and $Zn(CH_3COO)_2.2H_2O$ (≥ 99%) have been furnished by ROYALEX and Merck Companies, respectively. The details of procurement procedures of $TiO_2$ nanostructures have been introduced in Ref.[38]. To provide $TiO_2$ nanostructures, 20$^{cc}$ of NaOH (0.2 M) was dropwise added to 22$^{cc}$ of $TiCl_4$ in the liquid phase on a magnetic stirrer, and after evaluating the pH of the mixture, it was irradiated by microwaves at 800W for 10 min. The distilled water was employed to wash the resulting white mixture before drying at 25 °C. For synthesizing the $ZnTiO_3$ nano-powders, three separate beakers of $Zn(CH_3CO_2)_2$ (0.2 M), NaOH (0.2 M), and $TiO_2$ (0.15 M) solutions were initially made ready. Next, the solutions of $TiO_2$ and NaOH were dropwise added to $Zn(CH_3CO_2)_2$ solution at a temperature of 25 °C under ultrasonic irradiation. The product was placed in a microwave device and exposed to 800 W microwave radiation for 10 min. Then, the result was dried at the 25 °C temperature after rinsing during centrifugation. Eventually, the resulting nano-powder was annealed at the 700 °C temperature for 2 h. The preparation procedure of the $ZnTiO_3$ nanostructures is schematically shown in Fig. 1.

It should be noted that a p-type Si wafer with a 300 µm thickness was employed as a substrate in this research. To prepare PVP: $ZnTiO_3$ interfacial polymer layer, 10 mg of $ZnTiO_3$ nanostructures was dispersed by ultrasonic technique after providing a 5% solution of PVP with solvating 5 g of PVP nano-powders in 95$^{cc}$ water. Then, a thin layer of PVP: $ZnTiO_3$ with a thickness of 100 nm was deposited on the Si wafer using a spin coater system.

### UV-Vis spectroscopy

The UV–Vis spectroscopy was performed by Shimadzu UV-1800 in the wavelength range of 200–800 nm to determine the absorbance and transmittance of the $ZnTiO_3$ nanocomposite (see Fig. 2a). As can be seen, the absorbance of the $ZnTiO_3$ nanocomposite is decreased by raising the wavelength while the transmittance increases. In addition, Tauc's equation is used to determine the optical band gap of the $ZnTiO_3$ nanocomposite which is equal to 3.87 eV (see Fig. 2b)[38].

### SEM Image

The scanning electron microscope (SEM) (model LEO 1430 VP) at 15 kV accelerator voltage was utilized to record the SEM images to survey the morphology of the $ZnTiO_3$ nanocomposite. The surface-morphology schema of the prepared $ZnTiO_3$ nanocomposite is depicted in Fig. 3. Because of the difficulty of observing the sizes of actual particles, the structure of polydispersity nanoparticles appears in various configurations with an average size of <50 nm. Furthermore, all nanoparticles are clustered to form micron-sized clusters.

### Raman spectroscopy

A potent analytical method established on the inelastic scattering of light is Raman spectroscopy, enabling unmatched structural information on the atomic scale. A high-resolution Raman spectrometer system (inno-Ram™) was used in this research to record the Raman spectrum of the $ZnTiO_3$ nanocomposite. Based on the prediction of group theory (point group C3i), 10 Raman active modes are assigned to the $ZnTiO_3$, i.e., $5A_g + 5E_g$[39]. Figure 4 shows the Raman spectrum of $ZnTiO_3$ nanocomposite in the Raman shift of 140–800 $cm^{-1}$. The Raman vibrations of the $ZnTiO_3$ molecule were observed at the Raman shift of 152, 190, 225, 265, 346, 384, 477, 494, 619, and 724 $cm^{-1}$ corresponded to the symmetrical phonon modes of $E_g$, $A_g$, $E_g$, $A_g$, $A_g$, $E_g$, $E_g$, $A_g$, $E_g$, and $A_g$, respectively. These peaks confirm the presence of $ZnTiO_3$ nanostructure in the prepared PVP: $ZnTiO_3$ nanocomposite. However, the observation of noise in the Raman spectrum is due to the composite of the thin layer. It is necessary to mention that low-frequency vibration modes only appeared for the particles or crystallites at nanometric size[40]. So, four peaks at 152, 190, 225, and 265 $cm^{-1}$ corresponding to the Zn-Ti–O vibrational modes indicate the nanometric scale of the particles.

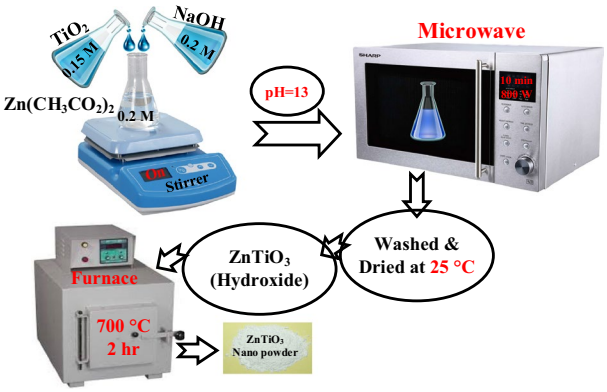



**Figure 1.** Schematic of the preparation procedure of $ZnTiO_3$ nano-powder.

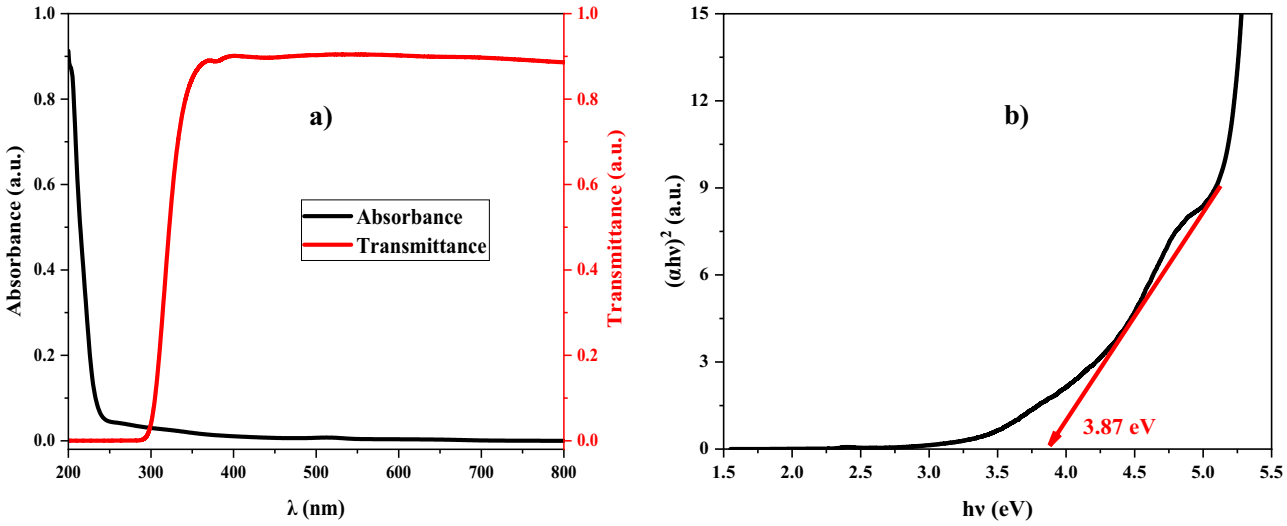



**Figure 2.** UV–Vis spectroscopy of PVP: $ZnTiO_3$ nanocomposite to study the (**a**) absorbance and transmittance, (**b**) profile of $(\alpha h\upsilon)^2$ versus hυ.

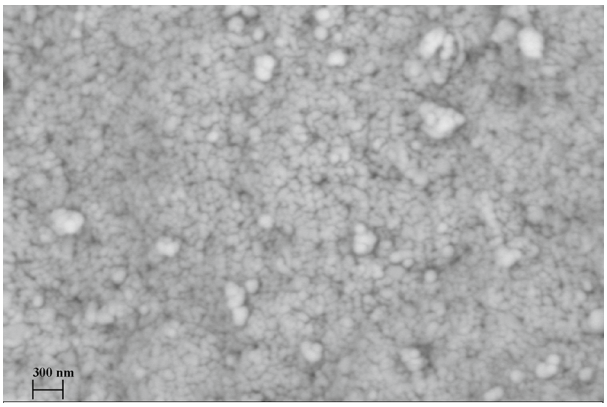



**Figure 3.** SEM image of the $ZnTiO_3$ nanocomposite.

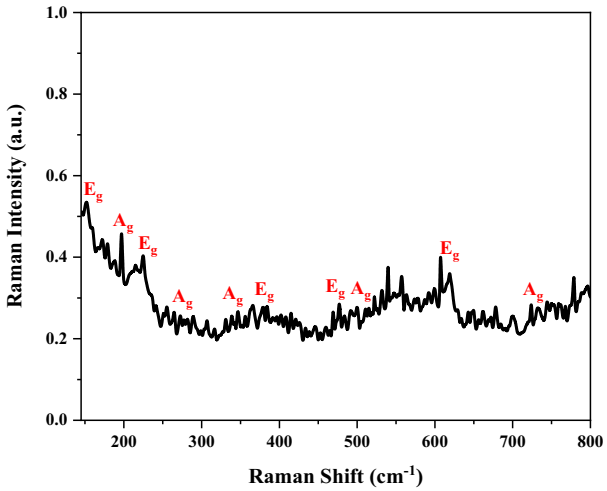



**Figure 4.** Raman spectrum of PVP: $ZnTiO_3$ nanocomposite.

## Attenuated total reflectance (ATR) & Fourier transform infra-red (FTIR) spectroscopy

ATR and FTIR spectroscopy methods are commonly applied for investigating the chemical identification of a desired sample. The ATR and FTIR spectra have been measured by BRUKER (vertex 80) device in this work. Figure 5 represents the ATR and FTIR spectra of PVP: $ZnTiO_3$ nanocomposite with the assignment of the primary ATR and FTIR bands. Since the distinctive bands of metal oxides (< 750 $cm^{-1}$) correspond to the bonds between metal and oxygen, the absorption band at the wavenumber range of 600–1000 $cm^{-1}$ is attributed to the Ti–O, O–Ti–O, Zn–O, O–Zn–O, and Zn–Ti–O linked to $ZnTiO_3$ species (see Fig. 5a). In more detail, the Ti–O bond vibrations are observed at the low wavenumber region from 400 to 650 $cm^{-1}$[41]. The Zn–Ti–O vibration modes were detected at 735 $cm^{-1}$. Moreover, the Ti–O octahedral absorption band appears at the wavenumber of 560 and 590 $cm^{-1}$. The bands at the wavenumber of 550–650 $cm^{-1}$ are assigned to $TiO_6$ vibration modes[42].

It is obvious that the bands at higher wavenumber regions are related to the $CH_2$ symmetric bending vibration, C–H asymmetric stretching vibration, and O–H stretching vibration corresponding to 2922, 2955, and 3496 $cm^{-1}$, respectively. It should be mentioned that the PVP is a macropolymer with $CH_2$, C=O, and C–N functional groups, consisting of a very hydrophilic part and large hydrophobic groups. Since water and several non-aqueous liquids are supreme solvents for PVP, water has been used to solve the PVP polymer nano-powder in this work and hence, the O–H group appears in the FTIR spectrum (see Fig. 5b)[35].

## Atomic force microscopy (AFM) image

The spectroscopic ellipsometry (SE) method is based on measuring the polarization of light after reflecting from a surface. It is generally accepted that optical elements do not depolarize light. However, there are certain circumstances where this assumption may not hold and depolarization can occur. For instance, when the light illuminates an area of the sample surface where the film thickness is non-uniform, it can lead to quasi-depolarization. Moreover, some of the light that reaches the polarization state detector may not have a distinguishable polarization state or cross-polarization may occur in systems that are theoretically isotropic if the sample is highly rough. On the other hand, atomic force microscopy (AFM) is an appropriate method to determine the surface roughness.

AFM, a form of scanning probe microscopy (SPM), has exhibited a resolution with an order of a nanometer compared to the optical diffraction limit. AFM uses the feeling of touching the surface with a mechanical probe to get the data. Piezoelectric components allow for small, exact movements under (electrical) control, enabling perfect scanning. It is possible to create a high-resolution image of the topography of a sample surface using the probe's response to the forces the sample imposes on it. In this work, an atomic force microscope (model WITec alpha300 A) has been employed to record the 3-dimensional shape of the surface of the PVP: $ZnTiO_3$ thin film. The topography of the $ZnTiO_3$ nanocomposite recorded by the AFM is represented in Fig. 6. As shown, since the $ZnTiO_3$ nanocomposite's surface roughness is ~ 1.05 nm, this nanocomposite thin film is smooth in the sub-nanometer scale.

## Spectroscopic ellipsometry (SE) method spectroscopy

The Spectroscopic Ellipsometry (SE) technique is typically a non-invasive, non-destructive measurement method that uses reflected light waves to determine a sample material's optical properties. The SE method does not require absolute intensity as long as the absolute intensity is sufficient because it assesses a relative change in polarization. The SE measurement is exceedingly accurate and repeatable as a result[43].

Ellipsometry makes use of the fact that linearly polarized light at an oblique incidence to a surface changes its polarization state when reflected. It is elliptically polarized, giving rise to the term "ellipsometry". In addition,

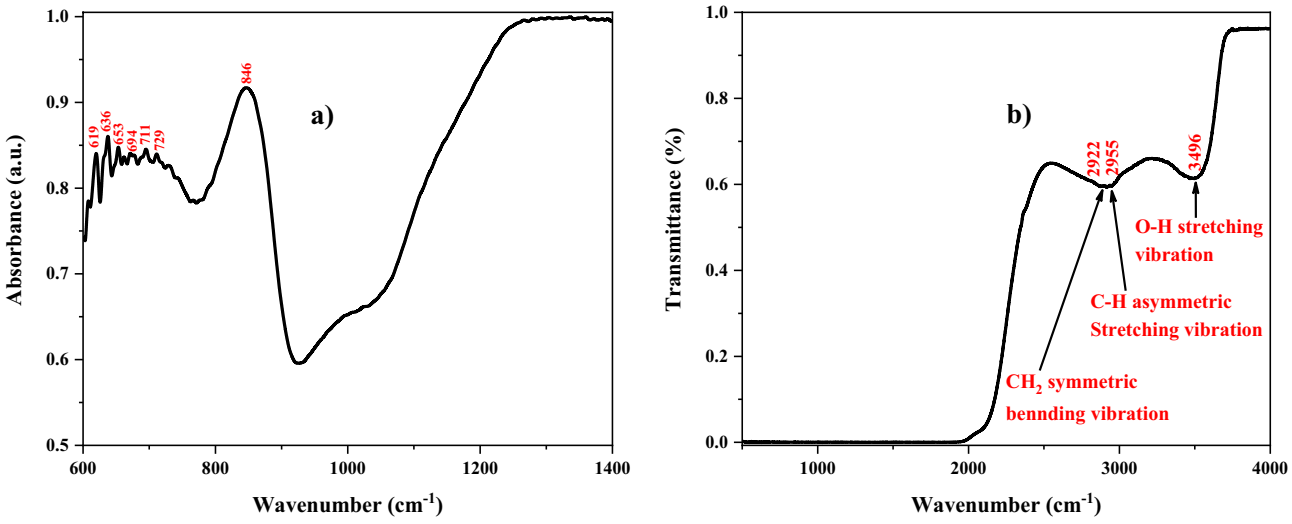



**Figure 5.** (**a**) ATR and (**b**) FTIR spectrum of PVP: $ZnTiO_3$ nanocomposite.

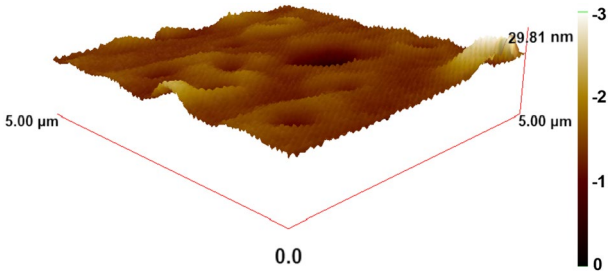



**Figure 6.** AFM image of the $ZnTiO_3$ nanocomposite.

the incident light wave might be elliptically polarized light in some circumstances. Figure 7 depicts the general concept of ellipsometry.

Once a monochromatic plane light wave is obliquely incident on a surface, the plane of incidence is defined as a plane perpendicular to the surface, including the vector pointing in the light wave's propagation direction[44]. This vector is referred to as the wavevector $\mathbf{k_{in}}$. The two mutually perpendicular vectors of the light wave's electric field **E** and magnetic field **B** are perpendicular to $\mathbf{k_{in}}$. The only vector displayed in Fig. 7 is the **E**-vector, which is selected to represent the polarization of the light wave. The **E**-vector is divided into two parts that are perpendicular to each other and perpendicular to $\mathbf{k_{in}}$[44]. Figure 7 shows how the two components of **E** are parallel and perpendicular to the plane of incidence. As observed, the ellipsometer used in this work consists of seven optical elements (1) light source, (2) light collimator, (3) polarizer, (4) sample ($ZnTiO_3$ nanocomposite), (5) phot-elastic modulator (PEM), (6) analyzer, and (7) detector.

The light wave that is incident to the surface is linearly polarized. The p- and s-components of the **E** field can be considered as oscillating with a specific amplitude and mutual phase whose endpoint moves in a straight line on the plane of p- and s-components[43]. The polarization of the light wave changes to an elliptical state after reflecting off the surface. As a result of the amplitude and mutual phase of the p- and s-components of **E** field changing, the endpoint of E moves in an ellipse. A detector can measure the ellipse's shape that is related to the ellipsometric parameters ψ and Δ by data processing. It should be mentioned that HORIBA (JOBIN YVON UVISEL 2) spectroscopic ellipsometer has been utilized in this work to get the ellipsometric parameters at the fixed incidence angle of 70° in room temperature. The ellipsometric parameters can be connected to the reflection coefficients of light polarized parallel and perpendicular to the plane of incidence[43].

Figure 8 illustrates the variations in the ellipsometric parameters (ψ and Δ) within the photon energy range of 0.59–4.59 eV. The experimental measurements of ψ and Δ have been analyzed not only through the NLR fitting process but also through the application of two ML algorithms, namely the ANN and SVR algorithms. As the figure shows, the fitting values are very close to the experimental ones.

To compare the obtained results more accurately, the R2 score criterion has been calculated separately for the mentioned methods. The R2 score essentially indicates the accuracy of the performed calculations, and the closer it is to the value of one, the more it signifies that the parameters considered in the algorithms were appropriate and the training was more comprehensive; Consequently, the mean deviation between the fitted values and the actual values is less. Moreover, the mean absolute error (MAE) is the other essential parameter in determining the accuracy of the analysis methods applied in this work. Table 1 introduces the value of the R2 score, MAE,

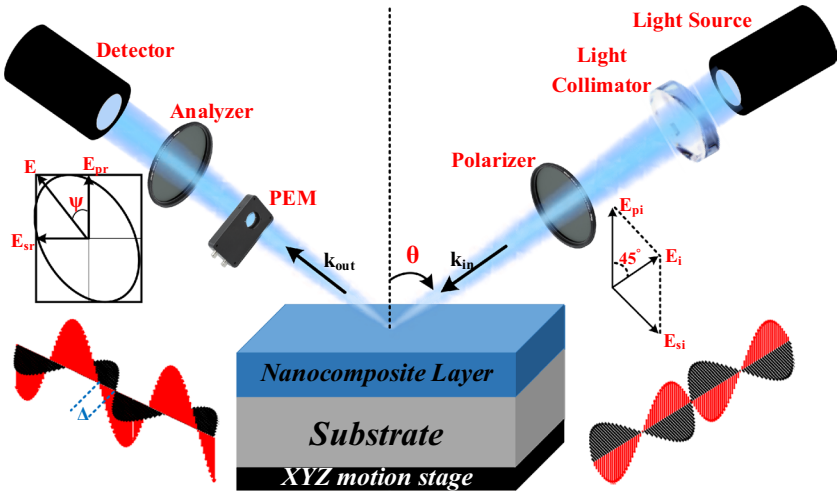



**Figure 7.** Schematic diagram of an ellipsometry setup.

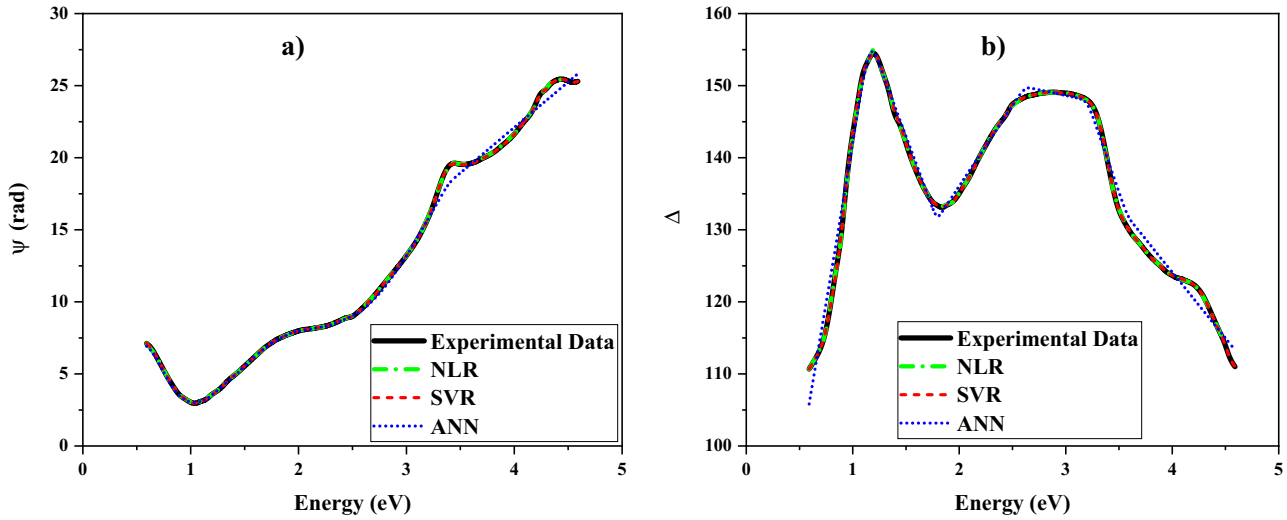



**Figure 8.** Experimentally measured ellipsometry parameters (**a**) Ψ and (**b**) Δ, compared with the spectra reconstructed by SVR, ANN, and by nonlinear regression (i.e., manual fitting).

| | ψ (rad) | | | Δ | | |
|---|---|---|---|---|---|---|
| **Algorithm** | **R2 Score** | **MAE** | **Time (s)** | **R2 Score** | **MAE** | **Time (s)** |
| NLR | 0.9998 | 0.0899 | 2.855 | 0.9962 | 0.7592 | 2.670 |
| ANN | 0.9973 | 0.2352 | 1.522 | 0.9852 | 1.1229 | 1.255 |
| SVR | 0.9999 | 0.0097 | 0.125 | 0.9999 | 0.0300 | 0.202 |

**Table 1.** The NLR, ANN, and SVR algorithms time to model in predicting the ellipsometric angles ψ and Δ.

and time needed to execute each of the applied algorithms for analyzing the ellipsometric parameters. The values of MAE and R2 score for the SVR algorithm are lower and higher than other algorithms in the analysis process, respectively. The time spent in ML algorithms for analyzing both ψ and Δ is lower than NLR. Moreover, the time spent in SVR is significantly lower compared to the other two algorithms.

## Results and discussion

The materials can be optically characterized via ellipsometric techniques. After illuminating the sample with a linearly polarized light beam, the reflected light is collected. To obtain the ellipsometric data, the amplitude ratio (ψ) of the parallel (p) and perpendicular (s) components of the reflected light, as well as the phase difference between them should be measured. The complex reflectance ratio (ρ) of the polarized light relates to the ψ and Δ ellipsometric parameters as[45]:

$$\rho = \frac{r_p}{r_s} = \tan(\Psi)\exp(i\Delta), \tag{1}$$

with $r_p$ and $r_s$ being Fresnel reflection coefficients of the reflected polarized light. The air-sample optical model to obtain the dielectric function is given by[45];

$$\varepsilon = \varepsilon_1 + i\varepsilon_2 = \varepsilon_0 sin^2(\varphi)\left[1 + \left(\frac{1-\rho}{1+\rho}\right)^2 tan^2(\varphi)\right], \tag{2}$$

where φ denotes the angle of incidence, $\varepsilon_0$ is the dielectric constant of air, and $\varepsilon_1$ and $\varepsilon_2$ refer to the real and imaginary parts of dielectric constants, respectively. Figure 9 represents changes of $\varepsilon_1$ and $\varepsilon_2$ parts of the complex dielectric function acquired by the analysis of ellipsometric data based on the air-sample optical model. There is a maximum in the spectrum of $\varepsilon_1$ at the photon energy of 3.24 eV. Moreover, a significant decreasing point is observed at photon energy 2 eV. Similar $\varepsilon_2$-spectrum behavior has previously been reported in numerous ellipsometry measurements on diverse samples[46–51]. There are two peaks in the $\varepsilon_2$-spectrum at 3.39 eV and 4.24 eV which are attributed to inter-band transitions or critical points (CPs).

Spectral-dependent refractive index (n) and extinction coefficient (k) are defined by using the spectra of $\varepsilon_1$ and $\varepsilon_2$ as follows[52]:

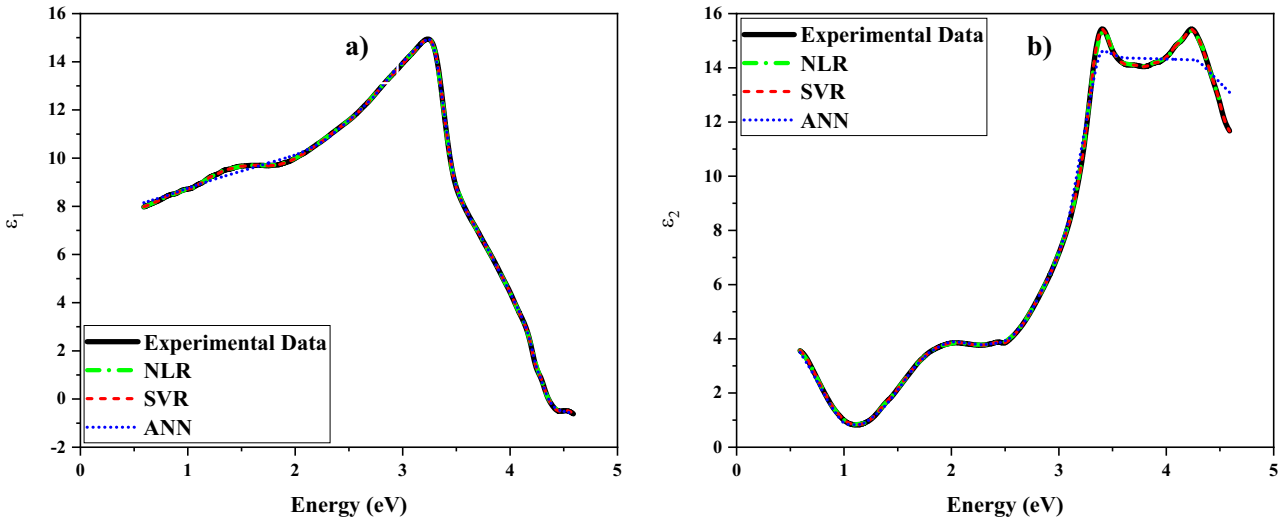



**Figure 9.** The energy-dependent (**a**) $\varepsilon_1$ and (**b**) $\varepsilon_2$ components of the dielectric function of $ZnTiO_3$ nanocomposite determined by SVR and ANN inferences and by nonlinear regression (manual fitting regression).

$$n = \left[\frac{\varepsilon_1 + \left(\varepsilon_1^2 + \varepsilon_2^2\right)^{1/2}}{2}\right]^{1/2}, \tag{3}$$

$$k = \left[\frac{-\varepsilon_1 + \left(\varepsilon_1^2 + \varepsilon_2^2\right)^{1/2}}{2}\right]^{1/2}. \tag{4}$$

Figure 10 shows the energy-dependent refractive index and extinction coefficient of the $ZnTiO_3$ nanocomposite. A peak in the extinction coefficient spectrum has appeared at the same energy position of the $\varepsilon_2$-spectrum. The band gap energy of the $ZnTiO_3$ nanocomposite was calculated to be 3.83 eV which is in good agreement with the $E_g$ values of 3.87 eV and 3.80 eV respectively introduced in refs.[6,53]. It can be observed that the value of the extinction coefficient is decreased at energies lower than the band gap energy. Additionally, the refractive index of the $ZnTiO_3$ nanocomposite is 3.24 at the band gap energy (~3.87 eV), and it changes between 3.16 and 4.15 at the visible spectral region, i.e., 1.77–3.26 eV. Based on the changes of $\varepsilon_2(\omega)$, the electron transitions from valence bands to conduction bands are what cause the peaks in the extinction and absorption coefficients (see Figs. 10, 11a).

After obtaining the refractive index and extinction coefficient of the $ZnTiO_3$ nanocomposite, the absorption coefficient α(E) and orthogonal incident reflectance R(E) could be derived as[54]:

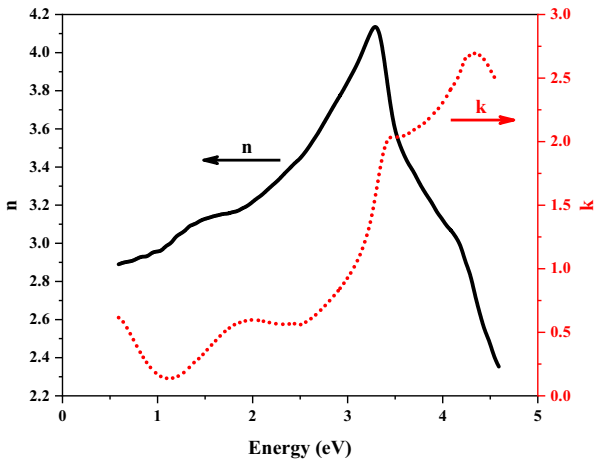



**Figure 10.** Spectral-dependent refractive index and extinction coefficient of the $ZnTiO_3$ nanocomposite.

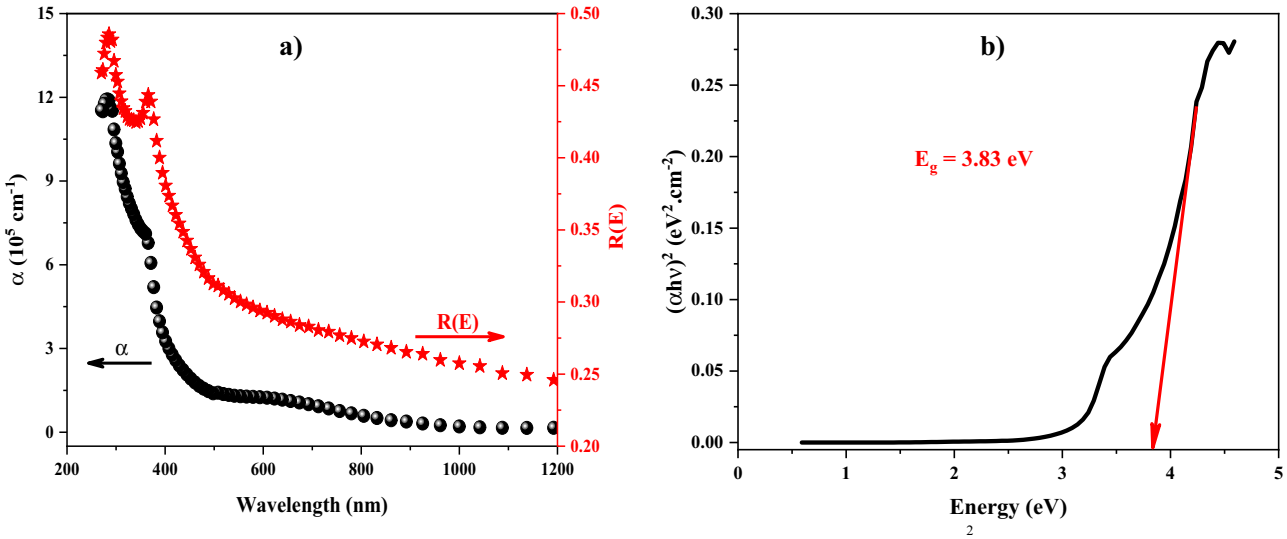



**Figure 11.** (**a**) Spectral dependencies of absorption and reflection coefficients, (**b**) $(\alpha h\nu)^2$ versus photon energy ($h\nu$).

$$\alpha(E) = \frac{4\pi}{\lambda}k(E), \tag{5}$$

$$R(E) = \frac{[n(E)-1]^2 + k^2(E)}{[n(E)+1]^2 + k^2(E)}. \tag{6}$$

It must be noted that SE measurements on any other faces besides the crystal's usual layer-plane face are extremely challenging due to the crystal's layer organization. It is appropriate to investigate the current SE measurement spectra using the binary phase (air/sample) instance. The spectral dependencies of the absorption coefficient (α) and the reflectance coefficient (R) are introduced in Fig. 11a. The absorption spectrum has a peak and a local maximum at the wavelength of 282 nm and 360 nm, respectively. The absorption coefficient is generally declined by increasing the wavelength and it is zero in the wavelength range of 1000–1100 nm. A similar behavior could be seen in the reflectance spectrum except for zero value at no wavelength. Furthermore, the absorption coefficient and band gap energy could be related to each other as follows[55]:

$$(\alpha h\upsilon) = A\left(h\upsilon - E_g\right)^m, \tag{7}$$

where m refers to a constant value which is 2 and 0.5 for indirect and direct transitions, respectively. Based on Eq. (7), if $(\alpha h\nu)^{1/m}$ is plotted as a function of $h\nu$ at the absorption edge region, the band gap energy ($E_g$) could be determined by the point where the fitted straight line intersects the energy axis. As can be seen from Fig. 11b, the indirect band gap energy for the $ZnTiO_3$ nanocomposite equals 3.83 eV, where the fitted straight line intersects the energy axis. This $E_g$ is in good agreement with the reported $E_g$ values for $ZnTiO_3$ nanocomposite[53]. These results were confirmed by the UV–Vis spectroscopy presented in Sect. 2.2.

According to Ref.[45], interband transition energies (also known as critical points, or CPs) could be examined by analysis of second-energy derivatives of different dielectric function components. Theoretically, the critical point energy ($E_{cp}$), photon energy (E), broadening parameter (Γ), amplitude (A), and phase angle (φ) relate to the second-energy derivative spectra of the components of the dielectric function as[45]:

$$\frac{d^2\varepsilon}{dE^2} = m(m-1)Ae^{i\varphi}\left(E - E_{cp} + i\Gamma\right)^{m-2} \text{ for } m \neq 0, \tag{8}$$

$$\frac{d^2\varepsilon}{dE^2} = Ae^{i\varphi}\left(E - E_{cp} + i\Gamma\right)^{-2} \text{ for } m = 0, \tag{9}$$

where m refers to the dimensions of the wave vectors involved in optical transitions. For excitonic, one, two, and three-dimensional lineshapes, the m values are 1, 1/2, 0, and + 1/2, respectively. The second-energy derivative spectra of $\varepsilon_1$ (circles) and $\varepsilon_2$ (stars) components are shown in Fig. 12. In the energy region, where the smoothing method has no effect on the main and first derivative spectra, a fitting process was used. As can be seen from Fig. 12, the fitting approach was used in this energy range because dielectric function components exhibit notable changes outside the 2.5–4.5 eV range.

The fitting applications had the lowest mean square deviations in the case of excitonic optical transitions (corresponding to m = -1). Six CP energies of 3.39, 3.72, 3.89, 4.09, 4.24, and 4.44 eV were obtained by fitting experimental data to theoretical definitions in the considered energy range. Near to CP energies are the observed

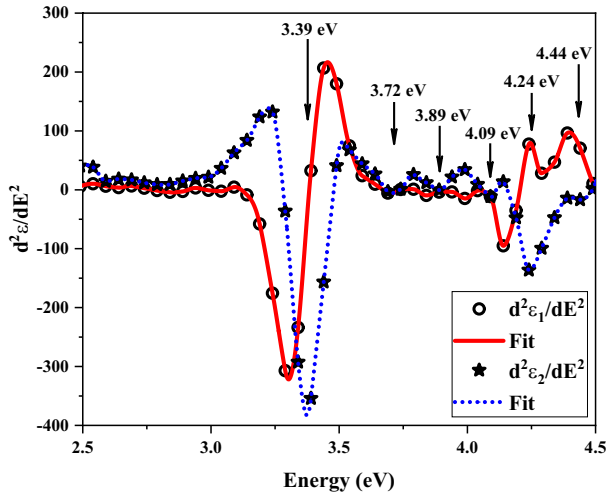



**Figure 12.** Second-derivative of the real and imaginary parts of dielectric function in terms of photon energy. Solid lines are the best fit.

local and absolute maximum values in the $\varepsilon_2$ spectrum. These CP energies show that the sample can absorb photons with these energies.

For additional analysis, the Wemple and DiDomenico single effective model and the Spitzer-Fan model have been used to examine the refractive index and real component of the dielectric function spectra. If the photon energy is lower than the band gap energy ($h\nu < E_g$), the refractive index could be expressed as follows using the Wemple and DiDomenico model[56]:

$$n^2(h\upsilon) = 1 + \frac{E_{so}E_d}{E_{so}^2 - (h\upsilon)^2}, \tag{10}$$

with $E_d$ and $E_{so}$ being the dispersion energy and single oscillator energy, respectively. $E_{so}$ is described as the average band gap energy, whereas $E_d$ corresponds to the intensity of the interband optical transition. To obtain the $E_d$ and $E_{so}$ values, the graph of $(n^2\text{-}1)^{-1}$ should be plotted as a function of $(h\nu)^2$ as shown in Fig. 13a. The slope and the intercept of the linear fit are applied for calculating the value of $E_d$ and $E_{so}$ energies equal to 33.1 and 4.43 eV, respectively. Moreover, the value of the refractive index ($n_0$) and dielectric constant ($\varepsilon_0$) at zero frequency ($\nu = 0$) could be computed by using definitions of $n_0 = (1 + E_d/E_{so})^{-1}$ and $\varepsilon_0 = n_0^2$ as 2.41 and 8.47, respectively.

The wavelength-dependent real part of the dielectric function ($\varepsilon_1$) is given by the Spitzer-Fan model as[57]

$$\varepsilon_1 = n^2 - k^2 = \varepsilon_\infty - \left(\frac{e^2}{\pi c^2}\right)\left(\frac{N}{m^*}\right)\lambda^2, \tag{11}$$

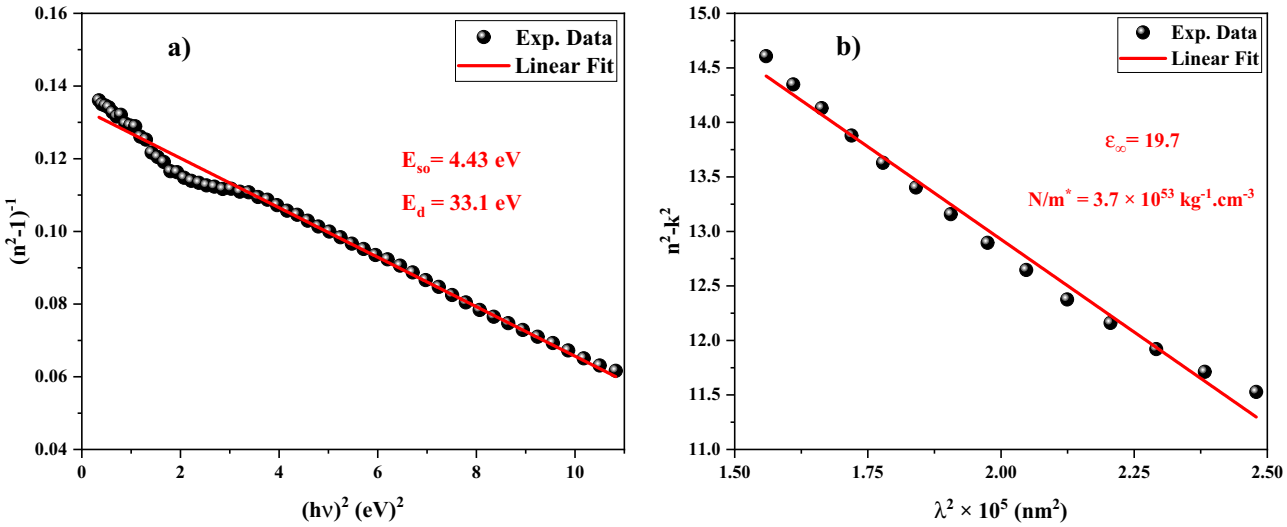



**Figure 13.** The plot of (**a**) $(n^2-1)^{-1}$ versus $(h\nu)^2$, and (**b**) $(n^2-k^2)$ versus $\lambda^2$.

where $\varepsilon_\infty$ refers to the dielectric constant at high frequencies, N denotes the carrier concentration, m* symbolizes the effective mass, c and e are the speed of light and electron charge. When $n^2$-$k^2$ is plotted in terms of $\lambda^2$ (see Fig. 13b), the slope and intercept of the linear fit are used to compute the values of $\varepsilon_\infty$ and N/m* found as 19.7 and $3.7 \times 10^{53}$ $kg^{-1}$ $cm^{-3}$, respectively.

Finally, it is useful to study the optical loss function, L(ω), and optical conductivity, σ(ω), which are defined using the dielectric function, ε(ω), as[58–60]:

$$L(\omega) = -Im\left(\frac{1}{\varepsilon(\omega)}\right) = \frac{\varepsilon_2(\omega)}{\varepsilon_1^2(\omega) + \varepsilon_2^2(\omega)}, \tag{12}$$

$$\sigma(\omega) = \sigma_1(\omega) + i\sigma_2(\omega) = -i\frac{\omega}{4\pi}(\varepsilon(\omega) - 1). \tag{13}$$

Figure 14a represents the loss function of the $ZnTiO_3$ nanocomposite. Generally, the energy-loss function, whose absolute maximum and matching frequencies are related to the plasma oscillations and the plasma frequency, depicts the energy loss when a fast electron passes in a material and deflects its route. As seen, the loss function of the $ZnTiO_3$ nanocomposite has no absolute maximum in the considered photon energy although there is an absolute minimum at the photon energy of 1.15 eV. Figure 14b reveals the spectral dependencies of the optical conductivity of the $ZnTiO_3$ nanocomposite in the considered photon energy. Optical conductivity consists of two components, i.e., $\sigma_1(\omega)$ and $\sigma_2(\omega)$, which are directly related to photocurrent and photoresistance[61,62]. As expected, the behavior of real and imaginary components of the optical conductivity and dielectric function are opposite. So, the $\varepsilon_2(\omega)$ directly gives the $\sigma_1(\omega)$ that indicates the absorption or energy loss in a material caused by light-induced electric current. The absorption or energy loss in the $ZnTiO_3$ nanocomposite increases with the increment of the photon energy till 4.4 eV, and it reduces after that. However, a relative reduction is observed in the absorption/loss after the photon energy of 3.45 eV. The inter-band transition between unoccupied and occupied states is the main reason for the appearance of the peaks in the $\sigma_1(\omega)$ spectra. On the other hand, the $\sigma_2(\omega)$ is obtained by the $\varepsilon_1(\omega)$, and it demonstrates the energy storage capacity of a material that is directly relevant to photoresistance. Therefore, the profile of the imaginary part of optical conductivity, $\sigma_2(\omega)$, shows that the energy storage capacity in the $ZnTiO_3$ nanocomposite is minimum at the photon energy of 3.4 eV.

## Conclusion

In this work, the spectroscopic ellipsometry method was employed to measure the optical properties of the PVP: $ZnTiO_3$ nanocomposite. The details of the preparation process of the $ZnTiO_3$ nanocomposite were described. UV–Vis spectroscopy, Field-Emission Scanning Electron Microscopy (FESEM), Raman spectroscopy, Attenuated Total Reflectance (ATR)-Fourier transform Infra-Red (FTIR), and Atomic Force Microscopy (AFM) were used to study the absorbance/transmittance, the surface morphology, structural information, chemical identification, and surface topography of the $ZnTiO_3$ nanocomposite, respectively. The energy of the optical band gap was calculated to be 3.87 eV. It was observed that the average size of the polydispersity nanostructures was less than 50 nm. According to the group theory prediction ($5E_g + 5A_g$), ten Raman active modes of the $ZnTiO_3$ appeared in the Raman shift of 140–800 $cm^{-1}$. The vibration modes of Ti–O, Zn-Ti–O, and $TiO_6$ were detected at the low wavenumber region 400–650 $cm^{-1}$. The functional groups of $CH_2$, C-H, and O–H were also observed at the wavenumber region of 2000–3700 $cm^{-1}$, relating to the PVP polymer and water molecules used as a solution in the preparing process of PVP: $ZnTiO_3$ nanocomposite. Moreover, the roughness of the $ZnTiO_3$ nanocomposite surface was ~ 1.05 nm, meaning the considered nanocomposite is smooth on the sub-nanometer scale.

The ellipsometric parameters (ψ and Δ) that were experimentally measured, were analyzed by the common NLR method and two algorithms of ML technique, i.e., ANN and SVR. This was done to demonstrate the

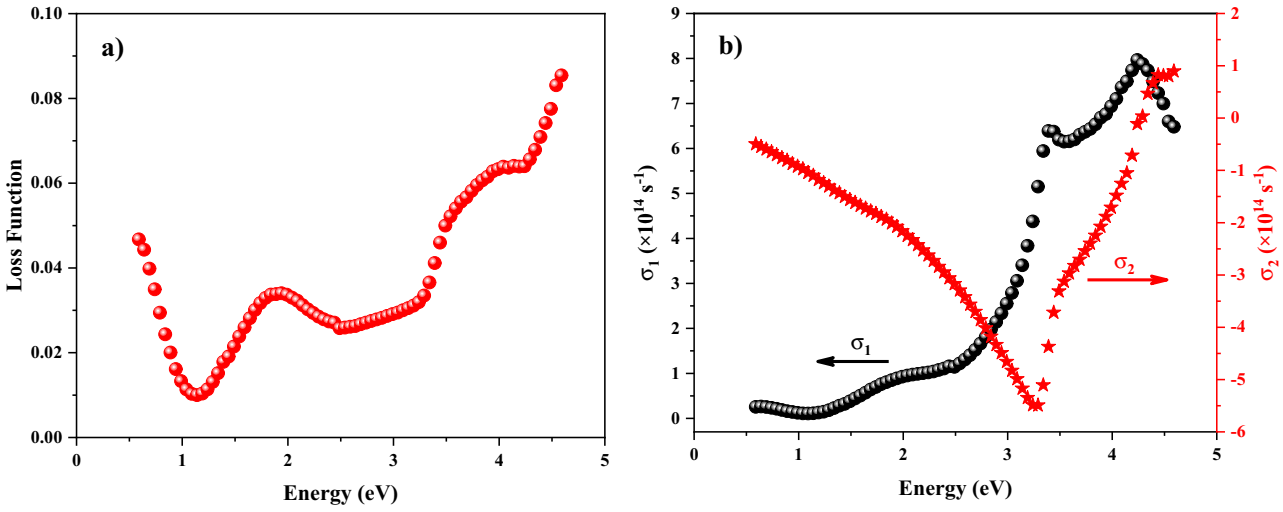



**Figure 14.** Spectral dependent (**a**) optical loss function and (**b**) optical conductivity.

efficiency of ML algorithms in ellipsometry data analysis. The obtained results show that the accuracy of data analysis using NLR, ANN, and SVR methods is very high and significant. Also, the values of the MAE and R2 score of the SVR algorithm are lower and higher than both other methods, respectively. On the other hand, the time required to analyze the ellipsometric data was calculated for all three methods. The comparison shows that the NLR method is time-consuming concerning the ANN and SVR methods. Moreover, the time needed for SVR is much less compared to the other two methods. Therefore, it can be concluded that ML algorithms can be a suitable alternative for ellipsometric data analysis, and the SVR method is preferred to the ANN method due to its low MAE, more accuracy, and less time consumption.

In addition, the spectral-dependent real and imaginary parts of the function ($\varepsilon = \varepsilon_1 + i\varepsilon_2$) and refractive index ($N = n + ik$) were measured by the ellipsometry method at the photon energy range of 0.59–4.59 eV. The energy-dependent absorption and reflectance coefficients of the $ZnTiO_3$ nanocomposite were obtained. It was found that the peaks that appeared in the absorption and extinction coefficients were due to the electron transitions from valence bands to conduction bands. Furthermore, the band gap energy of the $ZnTiO_3$ nanocomposite was computed as 3.83 eV using the absorption coefficient spectrum. The second-energy derivative of the dielectric function was applied to find the six critical point energies of the prepared sample in the energy range of 2.5–4.5 eV, indicating the sample can absorb photons at these energies. Based on the Wemple and DiDomenico model, the zero-frequency refractive index ($n_0$) and dielectric constant ($\varepsilon_0$) of the considered sample were calculated as 2.41 and 8.47, respectively. The high-frequency dielectric constant ($\varepsilon_\infty$) was obtained by the Spitzer-Fan model, equal to 19.7. At last, the spectral dependencies of the optical loss function and the optical conductivity of the $ZnTiO_3$ nanocomposite were studied.

## Data availability

The data that support the findings of this study are available from the corresponding author upon reasonable request.

Received: 18 October 2023; Accepted: 22 December 2023
Published online: 18 January 2024

## References

1. Naifar, A., Zeiri, N., Nasrallah, S. A. & Said, M. Linear and nonlinear optical properties of CdSe/ZnTe core/shell spherical quantum dots embedded in different dielectric matrices. *Photonics Nanostruct. Fundam. Appl.* **40**, 100789 (2020).
2. Piotrowski, P. & Pacuski, W. Photoluminescence of CdTe quantum wells doped with cobalt and iron. *J. Lumin.* **1**(221), 117047 (2020).
3. Azizian-Kalandaragh, Y., Sedaghatdoust-Bodagh, F. & Habibi-Yangjeh, A. Ultrasound-assisted preparation and characterization of β-$Bi_2O_3$ nanostructures: Exploring the photocatalytic activity against rhodamine B. *Superlattices Microstruct.* **1**(81), 151–160 (2015).
4. Zhao, X., Yang, H., Cui, Z., Li, R. & Feng, W. Enhanced photocatalytic performance of Ag–$Bi_4Ti_3O_{12}$ nanocomposites prepared by a photocatalytic reduction method. *Mater. Technol.* **32**(14), 870–880 (2017).
5. Afroz, K., Moniruddin, M., Bakranov, N., Kudaibergenov, S. & Nuraje, N. A heterojunction strategy to improve the visible light-sensitive water-splitting performance of photocatalytic materials. *J. Mater. Chem. A* **6**(44), 21696–21718 (2018).
6. Pirgholi-Givi, G., Azizian-Kalandaragh, Y. & Farazin, J. Comparison of the photocatalytic activity of perovskite structures: Bismuth, barium, and zinc titanate nanostructures for photodegradation of methylene blue from water. *J. Photochem. Photobiol. A* **1**(408), 113104 (2021).
7. Maeda, K. Rhodium-doped barium titanate perovskite as a stable p-type semiconductor photocatalyst for hydrogen evolution under visible light. *ACS Appl. Mater. Interfaces* **6**(3), 2167–2173 (2014).
8. Kulkarni, A. *et al.* Mixed ionic electronic conducting perovskite anode for direct carbon fuel cells. *Int. J. Hydrogen Energy* **37**(24), 19092–19102 (2012).
9. Singh, P., Kumar, A. & Kaur, D. ZnO nanocrystalline powder synthesized by ultrasonic mist-chemical vapor deposition. *Opt. Mater.* **30**(8), 1316–1322 (2008).
10. Singh, P., Kumar, A. & Kaur, D. Substrate effect on texture properties of nanocrystalline $TiO_2$ thin films. *Physica B* **403**(19–20), 3769–3773 (2008).
11. Wang, N. *et al.* Synthesis of ZnO/$TiO_2$ nanotube composite film by a two-step route. *Mater. Lett.* **62**(21–22), 3691–3693 (2008).
12. Rao, B. B. Zinc oxide ceramic semi-conductor gas sensor for ethanol vapour. *Mater. Chem. Phys.* **64**(1), 62–65 (2000).
13. Yoshino, Y., Makino, T., Katayama, Y. & Hata, T. Optimization of zinc oxide thin film for surface acoustic wave filters by radio frequency sputtering. *Vacuum* **59**(2–3), 538–545 (2000).
14. Jäger, S., Szyszka, B., Szczyrbowski, J. & Bräuer, G. Comparison of transparent conductive oxide thin films prepared by ac and dc reactive magnetron sputtering. *Surf. Coat. Technol.* **98**(1–3), 1304–1314 (1998).
15. Birkmire, R. W. & Eser, E. Polycrystalline thin film solar cells: present status and future potential. *Annu. Rev. Mater. Sci.* **27**(1), 625–653 (1997).
16. Look, D. C. Recent advances in ZnO materials and devices. *Mater. Sci. Eng. B* **80**(1–3), 383–387 (2001).
17. Bodade, A. B., Bende, A. M. & Chaudhari, G. N. Synthesis and characterization of CdO-doped nanocrystalline ZnO: $TiO_2$-based $H_2S$ gas sensor. *Vacuum* **82**(6), 588–593 (2008).
18. Zhang, X., Zhang, F. & Chan, K. Y. The synthesis of Pt-modified titanium dioxide thin films by microemulsion templating, their characterization and visible-light photocatalytic properties. *Mater. Chem. Phys.* **97**(2–3), 384–389 (2006).
19. Ke, S., Cheng, X., Wang, Q., Wang, Y. & Pan, Z. Preparation of a photocatalytic $TiO_2$/$ZnTiO_3$ coating on glazed ceramic tiles. *Ceram. Int.* **40**(6), 8891–8895 (2014).
20. Salavati-Niasari, M. *et al.* Synthesis, characterization, and morphological control of $ZnTiO_3$ nanoparticles through sol-gel processes and its photocatalyst application. *Adv. Powder Technol.* **27**(5), 2066–2075 (2016).
21. Lee, Y. C. & Chen, P. S. Effect of Cu dopant on microstructure and phase transformation of $ZnTiO_3$ thin films prepared by radio frequency magnetron sputtering. *Thin Solid Films* **520**(7), 2672–2678 (2012).
22. Li, Z. X., Shi, F. B., Ding, Y., Zhang, T. & Yan, C. H. Facile synthesis of highly ordered mesoporous $ZnTiO_3$ with crystalline walls by self-adjusting method. *Langmuir* **27**(23), 14589–14593 (2011).
23. Wu, S. P., Luo, J. H. & Cao, S. X. Microwave dielectric properties of $B_2O_3$-doped $ZnTiO_3$ ceramics made with sol–gel technique. *J. Alloys Compd.* **502**(1), 147–152 (2010).

24. Zhang, P. *et al.* $Bi_2MoO_6$ ultrathin nanosheets on $ZnTiO_3$ nanofibers: A 3D open hierarchical heterostructures synergistic system with enhanced visible-light-driven photocatalytic activity. *J. Hazard. Mater.* **30**(217), 422–428 (2012).
25. Wang, L., Kang, H., Xue, D. & Liu, C. Low-temperature synthesis of $ZnTiO_3$ nanopowders. *J. Cryst. Growth* **311**(3), 611–614 (2009).
26. Zhao, L., Liu, F., Wang, X., Zhang, Z. & Yan, J. Preparation and characterizations of $ZnTiO_3$ powders by sol–gel process. *J. Sol-Gel Sci. Technol.* **33**, 103–106 (2005).
27. Liu, X. Molten salt synthesis of $ZnTiO_3$ powders with around 100 nm grain size crystalline morphology. *Mater. Lett.* **1**(80), 69–71 (2012).
28. Yu, Y. H. & Xia, M. Preparation and characterization of $ZnTiO_3$ powders by sol–gel process. *Mater. Lett.* **15**(77), 10–12 (2012).
29. Chang, Y. S. *et al.* Synthesis, formation and characterization of $ZnTiO_3$ ceramics. *Ceram. Int.* **30**(8), 2183–2189 (2004).
30. Bobowska, I., Opasińska, A., Wypych, A. & Wojciechowski, P. Synthesis and dielectric investigations of $ZnTiO_3$ obtained by a soft chemistry route. *Mater. Chem. Phys.* **134**(1), 87–92 (2012).
31. Pal, N., Paul, M. & Bhaumik, A. New mesoporous perovskite $ZnTiO_3$ and its excellent catalytic activity in liquid phase organic transformations. *Appl. Catal. A Gen.* **393**(1–2), 153–160 (2011).
32. Sharma, M. & Tripathi, S. K. Frequency and voltage dependence of admittance characteristics of $Al/Al_2O_3$/PVA: n-ZnSe Schottky barrier diodes. *Mater. Sci. Semicond. Process.* **1**(41), 155–161 (2016).
33. Erbilen Tanrıkulu, E., Altındal, Ş & Azizian-Kalandaragh, Y. Preparation of (CuS–PVA) interlayer and the investigation their structural, morphological and optical properties and frequency dependent electrical characteristics of Au/(CuS–PVA)/n-Si (MPS) structures. *J. Mater. Sci. Mater. Electron.* **29**(14), 11801–11811 (2018).
34. Altındal, Ş *et al.* A comparison of electrical characteristics of Au/n-Si (MS) structures with PVC and (PVC: $Sm_2O_3$) polymer interlayer. *Phys. Scr.* **96**(12), 125838 (2021).
35. Koczkur, K. M., Mourdikoudis, S., Polavarapu, L. & Skrabalak, S. E. Polyvinylpyrrolidone (PVP) in nanoparticle synthesis. *Dalton Trans.* **44**(41), 17883–17905 (2015).
36. Samuel, A. L. Some studies in machine learning using the game of checkers. *IBM J. Res. Dev.* **3**(3), 210–229 (1959).
37. Vapnik, V. *The Nature of Statistical Learning Theory* (Springer, 1999).
38. Barkhordari, A. *et al.* The effect of PVP: $BaTiO_3$ interlayer on the conduction mechanism and electrical properties at MPS structures. *Phys. Scr.* **96**(8), 085805 (2021).
39. Baran, E. J. & Botto, I. L. Die Raman-Spektren von $ZnTiO_3$ und $CdTiO_3$. *Zeitschrift für anorganische und allgemeine Chemie* **448**(1), 188–192 (1979).
40. Hurma, T. & Kose, S. XRD Raman analysis and optical properties of CuS nanostructured film. *Optik* **127**(15), 6000–6006 (2016).
41. Last, J. T. Infrared-absorption studies on barium titanate and related materials. *Phys. Rev.* **105**(6), 1740 (1957).
42. Nolan, N. T., Seery, M. K. & Pillai, S. C. Crystallization and phase-transition characteristics of sol–gel-synthesized zinc titanates. *Chem. Mater.* **23**(6), 1496–1504 (2011).
43. Lindon, J. C., Tranter, G. E. & Koppenaal, D. *Encyclopedia of Spectroscopy and Spectrometry* (Academic Press, 2016).
44. Reitz, J. R., Milford, F. J. & Christy, R. W. *Foundations of Electromagnetic Theory* 4th edn. (Addison-Wesley, 1993).
45. Fujiwara, H. *Spectroscopic Ellipsometry: Principles and Applications* (Wiley, 2007).
46. Isik, M., Gasanly, N. M. & Turan, R. Spectroscopic ellipsometry study of above-band gap optical constants of layered structured $TlGaSe_2$, $TlGaS_2$ and $TlInS_2$ single crystals. *Phys. B Condens. Matter* **407**(21), 4193–4197 (2012).
47. Kock, I., Edler, T. & Mayr, S. G. Growth behavior and intrinsic properties of vapor-deposited iron palladium thin films. *J. Appl. Phys.* **103**(4), 528–587 (2008).
48. Pakizeh, E. Electronic and optical properties of $ZnCl_4H_2Me_2$biim polymeric complexes (DFT study). *J. Green Polym.* **1**(1), 6–10 (2023).
49. Pakizeh, E. Optical response and structural properties of Fe-doped Pb $(Zr_{0.52}Ti_{0.48})$ $O_3$ nanopowders. *J. Mater. Sci. Mater. Electron.* **31**(6), 4872–4881 (2020).
50. Pakizeh, E., Mohammadi, M. & Mostafaei, A. Effect of Hydrogen concentration on the structural, electronic and optical properties of 2D monolayer MXenes: DFT study. *Solid State Commun.* **1**(369), 115214 (2023).
51. Pakizeh, E., Jalilian, J. & Mohammadi, M. Electronic, optical and thermoelectric properties of Fe 2 ZrP compound determined via first-principles calculations. *RSC Adv.* **9**(44), 25900–25911 (2019).
52. Fox, M. *Optical Properties of Solids* (Oxford University Press, 2001).
53. Barkhordari, A., Mashayekhi, H. R., Amiri, P., Altındal, Ş & Azizian-Kalandaragh, Y. Role of graphene nanoparticles on the electrophysical processes in PVP and PVP: $ZnTiO_3$ polymer layers at Schottky diode (SD). *Semicond. Sci. Technol.* **38**(7), 075002 (2023).
54. Adachi, S., Adachi, S. *The Interband Transition Region: Amorphous and Microcrystalline Materials. Optical Properties of Crystalline and Amorphous Semiconductors: Materials and Fundamental Principles.* 1999;131–177.
55. Barkhordari, A. *et al.* The influence of PVC and (PVC: SnS) interfacial polymer layers on the electric and dielectric properties of Au/n-Si structure. *Silicon* **15**(2), 855–865 (2023).
56. Wemple, S. H. & DiDomenico, M. Jr. Behavior of the electronic dielectric constant in covalent and ionic materials. *Phys. Rev. B* **3**(4), 1338 (1971).
57. Spitzer, W. G. & Fan, H. Y. Determination of optical constants and carrier effective mass of semiconductors. *Phys. Rev.* **106**(5), 882 (1957).
58. Fang, R. C. *Solid Spectroscopy* (Chinese Science Technology University Press, 2003).
59. Zhang, Y. & Shen, W. M. *Basic of Solid Electronics* (Zhe-Jiang University Press, 2005).
60. Okoye, C. M. Theoretical study of the electronic structure, chemical bonding and optical properties of $KNbO_3$ in the paraelectric cubic phase. *J. Phys. Condens. Matter* **15**(35), 5945 (2003).
61. Jariwala, D., Davoyan, A. R., Wong, J. & Atwater, H. A. Van der Waals materials for atomically-thin photovoltaics: promise and outlook. *ACS Photonics* **4**(12), 2962–2970 (2017).
62. Song, B. *et al.* Complex optical conductivity of two-dimensional MOS2: A striking layer dependency. *J. Phys. Chem. Lett.* **10**(20), 6246–6252 (2019).


## Acknowledgements

This work was supported by the Presidency of Turkey, Presidency of Strategy and Budget with 2019K12-149045 project number.

## Author contributions

A.B., Conceptualization, Experiments, Formal analysis, Discussion, Writing - original draft; H.R.M., Supervision, Investigation, Writing—review and editing; P.A., Supervision, Writing—review and editing; S.Ö., Supervision, Writing—review and editing; F.H., Experiments; Y.A.-K., Methodology, Supervision, Project administration, Writing—review and editing. All authors reviewed the manuscript.

## Competing interests
The authors declare no competing interests.

## Additional information
**Correspondence** and requests for materials should be addressed to A.B.

**Reprints and permissions information** is available at www.nature.com/reprints.

**Publisher's note** Springer Nature remains neutral with regard to jurisdictional claims in published maps and institutional affiliations.

**Open Access** This article is licensed under a Creative Commons Attribution 4.0 International License, which permits use, sharing, adaptation, distribution and reproduction in any medium or format, as long as you give appropriate credit to the original author(s) and the source, provide a link to the Creative Commons licence, and indicate if changes were made. The images or other third party material in this article are included in the article's Creative Commons licence, unless indicated otherwise in a credit line to the material. If material is not included in the article's Creative Commons licence and your intended use is not permitted by statutory regulation or exceeds the permitted use, you will need to obtain permission directly from the copyright holder. To view a copy of this licence, visit http://creativecommons.org/licenses/by/4.0/.

© The Author(s) 2024